HYBRID PROFILES IN RADAR IMAGING


A Thesis


Presented in Partial Fulfillment of the Requirements for

Graduation with Distinction from the Department of Electrical Engineering

of The Ohio State University

by

Derek Gerlach

and

Dr. Randolph Moses, advisor

* * * * *

The Ohio State University

1990


Examination Committee:                              Approved by

Randolph Moses

Frederick Garber                    _____

Robert Garbacz                                      Advisor

                                    Department of Electrical Engineering

## ACKNOWLEDGEMENTS

I wish to thank Dr. Randolph Moses of The Ohio State University, for his guidance and helpful suggestions, and Donald Wehner of the Naval Ocean Systems Center, for his support and fruitful discussions. I also thank Dr. Robert Garbacz and Dr. Frederick Garber of the examination committee. Special regards to Professor Fred Harris of the San Diego State University.

LIST OF FIGURES

TABLE OF CONTENTS

CHAPTER I

INTRODUCTORY MATERIAL


## Introduction

The radar cross section (RCS) of a target is an indication of the target's
"brightness" or reflectivity at microwave frequencies [1,2]. The RCS of a
target is a function of the rotation angle of the target. Its value at a given
angle determines how visible a target will be to a microwave radar at that
rotation angle. To make a target more elusive, designers strive for a low RCS
over wide angular intervals.

On most radar targets, there are highly localized and reflective regions
known as scattering centers. Most of the contributions to the total RCS come
from scattering centers; therefore, to reduce the RCS, each scattering
center's strength must be minimized.  To gauge the success of existing
designs, and to guide future designs, knowledge of the strength and location
of each scattering center on the target is needed. It is therefore of interest
to compute the RCS distribution of a target, which is a two-dimensional
function indicating the sources of RCS on a three-dimensional target in a
known image plane. (An image of a given target is the projection of the
target's scatterers onto a plane. The plane onto which the projection occurs
is the image plane.) When the RCS distribution is integrated over the image
plane, the total RCS of the target results. The RCS distribution therefore not
only indicates the overall brightness of a target, but it also gives the
locations and amplitudes of the scattering sources.

1

One important property of scattering centers is that they tend to be visible over small intervals (typically 5-30$^\circ$ of angular rotation) [1]. That is, as the rotation angle is changed, a given scatterer may become visible and even vary in intensity over 5-30$^\circ$ before finally disappearing.

One technique for localizing scatterers on the image plane is by use of inverse synthetic aperture radar, or ISAR [1,3,4]. In ISAR processing, coherent data is collected over an angular interval typically 1-2$^\circ$ wide. This data is processed to form an RCS distribution using the two-dimensional DFT or similar algorithm [1]. However, ISAR processing is not always appropriate for the scattering center localization problem. There are two main reasons for this. First, ISAR processing is performed over a narrow angular interval, and a given scattering center may not be present or detectable in that interval. We require the localization of the scattering centers regardless of the angular interval in which they occur. Second, the image plane upon which the ISAR produces the RCS distribution is not always known. The image plane normal vector is a linear combination of the target rotation vector and the radar line of sight vector [1]. In many practical situations the rotation vector is not known, so the image plane is also unknown.

To overcome these problems, a tomographic approach of estimating the RCS distribution was developed in [5]. In this method, tomographic cross-range projections of the target's RCS distribution function were formed over a wide angular interval. The image was then reconstructed based upon the projections using the convolution-backprojection algorithm. The main drawback of this method is that it exhibits poor down-range resolution when imaging scattering centers in existence for angular intervals less than 60$^\circ$. Most scatterers are in existence for less than 60$^\circ$, producing distorted images.

In this paper, the method of [5] is extended to improve the down-range resolution. We present a method of locating the main sources of RCS,

2

regardless of the angular interval over which they are present; moreover, this method locates the scattering sources in a known image plane. The image itself is a wide-angle RCS distribution, based upon $180^\circ$ or more of angular interval. As before, a tomographic approach is used, but instead of using only cross-range projections, a new method involving hybrid projections is used. A hybrid projection is a variation of a cross- or down-range projection; it utilizes change in pulse frequency as well as angular diversity. This method is designed to accurately image scatterers which may exist for only $5-10^\circ$.

Because large rotation angles are used, the method described here is limited to cooperative targets or turntable models, rather than targets in a tactical situation. (The cooperation is needed to provide a large angle change, not a known rotation vector.)  This algorithm is well-suited for fixing the locations of the sources of RCS on a cooperative target.


Notation

$\theta$  = rotation angle of target.

f  = frequency of a pulse.

$f_x$  = $f\cos\theta$.

$f_y$  = $f\sin\theta$.

$\theta_o$  = rotation angle of first data point used to form a hybrid projection.

$f_o$  = radial frequency of the first data point used in the formation of a hybrid profile. ($f_o{}^2 = f_x{}^2 + f_y{}^2$)

$f_{xo}$ = $f_x$-component of the radial frequency $f_o$.

$f_{yo}$ = $f_y$-component of the radial frequency $f_o$.

$\alpha$  = projection angle of a projection.

$\Delta f$ = point to point change in frequency for data points used to form a hybrid profile. (Not radial change, but along the direction of transform.)

$\Delta f_x = \Delta f\cos\alpha$.

3

$\Delta f_y = \Delta f \sin\alpha$.

N   = number of angular increments used to form each projection (=size of the Fourier transform).

M   = number of projections used in forming the image.

$\Delta f_o$ = radial change in frequency between each profile used in the noncoherent average to reduce speckle.

L   = number of hybrid profiles which are averaged noncoherently to reduce speckle.

d   = distance between the radar and the target.

c   = speed of light.

g(x,y) = reflectivity density function of the target.

## DATA COLLECTION

The experimental setup considered here consists of a microwave radar illuminating a rotating target with a stepped frequency waveform, as shown in fig.1. The target is fixed with respect to the x-y axis and rotates with respect to the u-v axis. The radar is fixed on the u-axis a distance d from the origin. The target begins at a certain initial rotation angle $\theta_o$, and the radar transmits a pulse of frequency $f=f_o$. The pulse propagates to the target, engulfs its entire length, and is reflected back to the radar. The radar measures and records the baseband in-phase and quadrature component of the return pulse. The radar then transmits a pulse of frequency $f=f_o+\Delta f$, and repeats the same measurement, while the target remains at its same initial rotation angle. This process is repeated for each frequency through $f=f_o+\Delta f(S-1)$, with S equal to the number of frequency increments.

Next, the target rotates with respect to the u-v axis through an angle $\Delta\theta$, and the entire set of S I-Q frequency measurements are repeated at this new angle $\theta=\theta_o+\Delta\theta$. This process is repeated for each angle through $\theta=\theta_o+\Delta\theta(R-1)$, with R equal to the number of angular increments. In this manner, we tabulate an annular locus of known data points in data ($\theta$-f) space, as in fig.2. In our

4
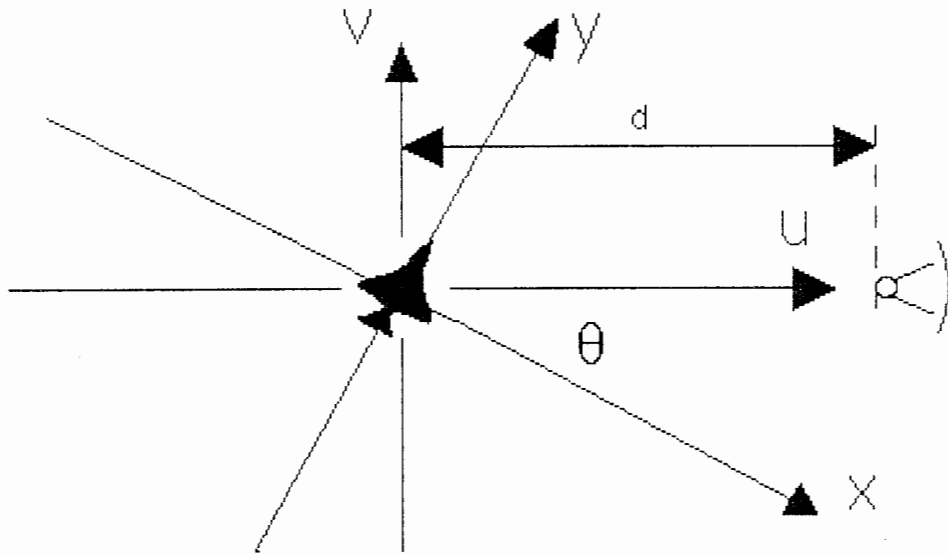
Figure 1. The physical setup. Since the radar is fixed to the u-v axis, the u-axis is the direction of down range.
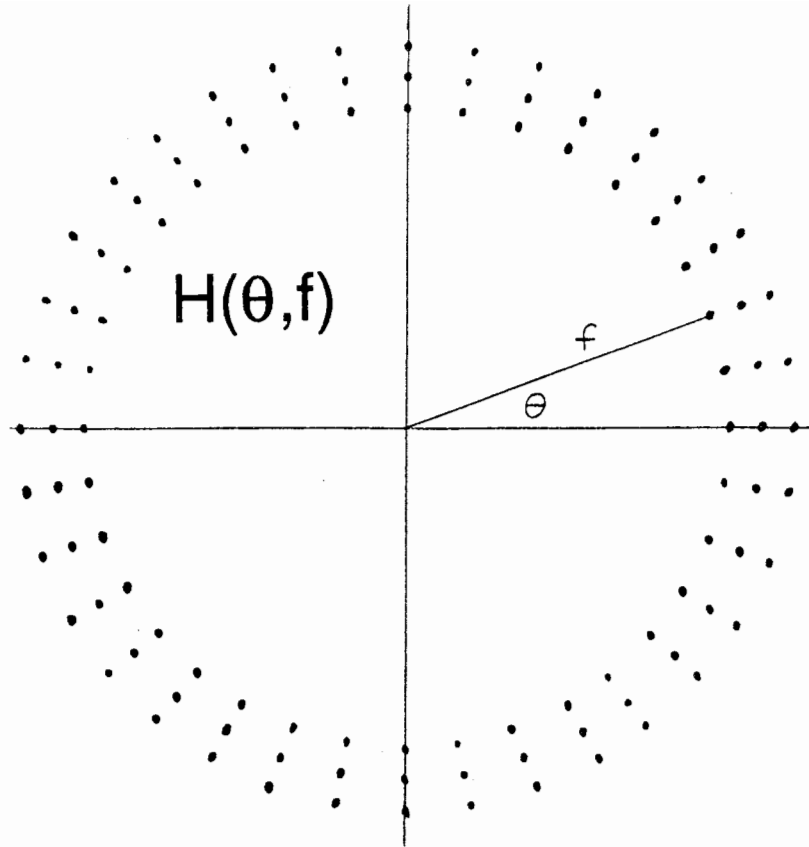
Figure 2. The locus of known I-Q reflectivity samples.

situation, R is chosen large enough so that the target rotates through a full circle. The problem is to find the distribution of scattering centers based upon this annular data. In this case, the image plane is the plane in which the target rotates.

The above measurement procedure was described for a turntable target; however, the process can be extended to actual moving targets as well. Instead of a turntable providing the change in rotation angle, the target's progression in a circular path will effectively yield the same rotation angle change. The problem of imaging "live" targets in this manner is considerably more difficult because, a) the target is translating as well as rotating, b) the target's rotation axis changes as a result of roll and pitch variations in the yaw motion, and c) the target's rotation angle is not fixed during the transmission of each burst. Because of these difficulties, experimental results presented here are based on turntable models, rather than such live measurements.

# CHAPTER II

## THE PROCESSING ALGORITHM

### Introduction

Let the target be represented by the reflectivity density function $g(x,y)$. The function $g^2(x,y)$ is the target's RCS distribution [1]. The goal of the algorithm described in this paper is to reconstruct $g^2(x,y)$ based upon the annular data region (or a subset thereof) shown in fig.2. This goal is achieved in a two-step process:

1) Obtain tomographic projections of $g(x,y)$. A tomographic projection of g at projection angle $\alpha$ is defined as

$$p_\alpha(s) = \int_{t=-\infty}^{+\infty} g(s \cos \alpha - t \sin \alpha, t \cos \alpha + s \sin \alpha)\, dt \tag{1}$$

As shown in fig.3, the s-t coordinate system is rotated an angle $\alpha$ with respect to the x-y coordinate system, so that

$$x = s \cos \alpha - t \sin \alpha$$
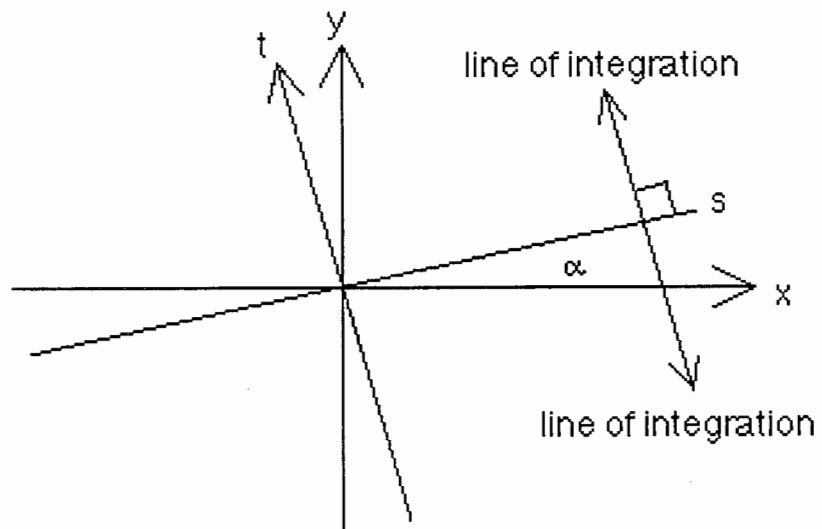$$y = s \sin \alpha + t \cos \alpha \tag{2a,b}$$

Figure 3. A typical integration path used in forming a tomographic projection.

The integration of (1) occurs along lines parallel to the t-axis, as a function of position on the s-axis.

2) Reconstruct $g^2(x,y)$ using the projections made in step one. The convolution-backprojection algorithm, a common tomographic reconstruction algorithm, is used to perform the reconstruction [7].

The convolution-backprojection algorithm requires significant diversity in the angles at which the projections are made in order to produce accurate reconstruction. One difficulty with this requirement is that some scattering centers of the target are in existence for a limited rotation angle (5-30$^{\circ}$, as mentioned earlier), making a large projection angle diversity difficult to obtain. However, the hybrid profile method developed below is able to achieve the projection angle diversity without the need for wide rotation angle diversity, giving rise to improved image quality.

The main contribution of this work is the development of improved ways of carrying out step one. These improvements allow the formation of projections spanning a wide range of projection angles, while using a narrow range of rotation angles. The key idea in generating these types of projections is the hybrid profile. A hybrid profile can be best understood by considering its relation to down-range and cross-range profiles. A down-range profile is formed by transforming radially in $\theta$-f space; that is, data points corresponding to the same rotation angle and increasing frequency are transformed with the discrete Fourier transform (DFT). The separation of scatterers occurs in the down-range direction. Likewise, a cross-range profile is formed by transforming along a circumference in data space: varying rotation angle but maintaining constant frequency. A hybrid profile is formed by transforming data points so that both angle and frequency are traversed from data point to data point. As will be shown, a hybrid profile separates

10

scatterers according to some "hybrid" direction, which is perpendicular to the direction of transform in data space. Transforming so both angle and frequency are traversed allows more diversity in the projection angle than if only angle or frequency is traversed.

In earlier work [5], a similar method of reconstructing $g^2(x,y)$ using tomographic projections was explored. However, this method used cross-range profiles only, so far less diversity in the projection angle was obtained. The lack of diversity gave rise to good resolution in the cross-range direction, but poor resolution in the down-range direction.

In this section we will also discuss the zero reference problem for the hybrid profiles. Convolution-backprojection requires that the origin of each projection corresponds to the same point on the target. Out of convenience, this point is chosen to be the center of rotation. We discuss a method of correcting the profiles so the center of rotation is coincident with the origin.

Speckle is unwanted destructive and constructive interference occurring between scatterers within the same resolution cell. Speckle occurs in the formation of hybrid profiles, and some method of reducing its effects is needed. The nature and solution of the speckle problem is well known [6,8], and is also addressed in this section.

## Preliminaries: The Reflectivity Density Function, The RCS Distribution Function, and The Target Response Function

In this section, we introduce three fundamental concepts key to the understanding of the imaging algorithm: the reflectivity density function, the RCS distribution, and the target response function.

First, assume the target is composed of a linear combination of ideal point scatterers. The target is represented by a reflectivity density function of the form

11

$$g(x, y) = \sum_i A_i \delta(x - x_i, y - y_i)$$

The quantity $A_i$ is the real, positive amplitude of the $i^{th}$ scatterer located at $(x_i, y_i)$. Moreover, assume g is space-limited, so that a frequency-domain-sampled representation of g is possible.

Second, since g is the reflectivity density function, giving the voltage gain as a function of position on the target, $g^2$ gives the power gain, and is called the RCS distribution. In practice, the delta functions of g(x,y) have non-zero width, so that $g^2(x,y)$ is a legitimate function.

Lastly, we will derive an expression for the target response function $(H_\theta(f))$ of a target represented by the reflectivity density function g(x,y). The response function of a target is the baseband I-Q measurement as a function of rotation angle and frequency at which the measurement was taken.

The derivation of the response function is as follows. Consider momentarily a target composed of a single point scatterer located at (x,y). Under far-field conditions, the response function at an angle $\theta$ and frequency f is given by:

$$H_\theta(f) = A e^{j 2\pi \frac{2}{\lambda} [d - x \cos \theta - y \sin \theta]}$$
$$= A e^{j \frac{4 \pi f}{c} [d - x \cos \theta - y \sin \theta]}$$

The scaler A is equal to the scatterer's amplitude, and the quantity d-xcos($\theta$)-ysin($\theta$) is the scatterer's down-range position. Since there is more than one scatterer, the linearity of the system implies that the total target response is
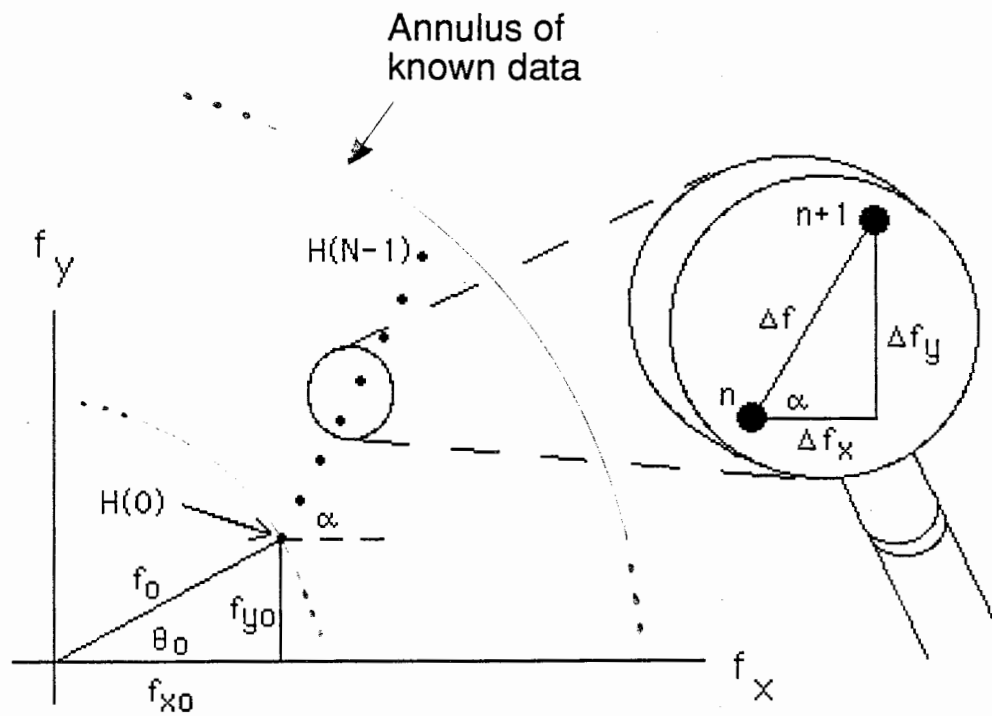
Figure 4. A set of points in dataspace used in the formation of a hybrid profile.

of points shown in fig.4, lying within the annulus of known data. The sequence H(n) is equal to the value of $H(f_x, f_y)$ at the points indicated in fig.4, so that

$$H(n) = H\left(f_{xo} + \Delta f_x \cdot n, f_{yo} + \Delta f_y \cdot n\right) \; ; \quad n = 0, ..., N-1$$
$$= 0 \qquad\qquad\qquad\qquad ; \quad \text{else} \qquad (5)$$

The quantities $f_{xo}, f_{yo}, \Delta f_x$, and $\Delta f_x$ are defined in the notation section of Chapter I, as well as in Fig.4. The hybrid profile is defined as

$$h(k) = N - \text{point} \quad \text{DFT}[H(n)] \; ; k = 0, ..., N-1$$
$$= 0 \qquad\qquad\qquad ; \text{else} \qquad (6)$$

The hybrid profile is analogous to a down- or cross-range profile, but it separates scatterers according to "hybrid" range, instead of down or cross range.

The hybrid profile is parametrized by $\alpha, \theta_o, \Delta f$, and $f_o$. By appropriately interpolating the frequency domain data, there need not be any restriction on the data points used in the transform, provided they lie within the annular region of data space. In this spirit, we assume $H(f_x, f_y)$ is available over the entire annular region. From the definition of H and the geometry of fig.4, (6) becomes

$$h(k) = \text{DFT}_N\left\{H\left(f_{xo} + \Delta f_x \cdot n, f_{yo} + \Delta f_y \cdot n\right)\right\}$$

$$= \text{DFT}_N\left\{e^{i\frac{4\pi f}{c}d} \int_{y=-\infty}^{+\infty} \int_{x=-\infty}^{+\infty} g(x, y)e^{-i\frac{4\pi}{c}\left[x(f_{xo} + \Delta f_x n) + y(f_{yo} + \Delta f_y n)\right]} \, dxdy\right\}$$

15

$$= DFT_N \left\{ e^{j\frac{4\pi f}{c}d} \int_{y=-\infty}^{+\infty} \int_{x=-\infty}^{+\infty} g(x, y) e^{-j\frac{4\pi}{c}\left[ f_o(x \cos \theta_o + y \sin \theta_o) + n\Delta f (x \cos \alpha + y \sin \alpha) \right]} dxdy \right\}$$

$$(7)$$

The quantity

$$u = x \cos \theta_o + y \sin \theta_o$$

in (7) can be interpreted as the displacement of a scatterer along the u-axis, as shown in fig.1. Likewise, the quantity

$$s = x \cos \alpha + y \sin \alpha$$

is the displacement of a scatterer along an axis rotated $\alpha$ degrees with respect to the x-y axis, as shown fig.3. As will be shown later, the quantity s is for a hybrid profile what down range is for a down-range profile, or what cross range is to a cross-range profile.

We now have for h(k)

$$h(k) = DFT_N \left\{ e^{j\frac{4\pi f}{c}d} \int_{x=-\infty}^{+\infty} \int_{y=-\infty}^{+\infty} g(x, y) e^{-j\frac{4\pi}{c}\left( f_o u + n\Delta f \cdot s \right)} dxdy \right\}$$

$$(8)$$

The frequency, f, in (8) is n-dependent. The n-dependence can be made explicit as follows:

$$f^2 = f_x^2 + f_y^2$$

$$= \left( f_{xo} + \Delta f_x n \right)^2 + \left( f_{yo} + \Delta f_y n \right)^2$$

16

$$= f_o^2 + \cos(\theta_o - \alpha)f_o \Delta f \cdot n + \Delta f^2 n^2$$

$$= \left(f_o + n\Delta f \cos(\theta_o - \alpha)\right)^2 + \left(n\Delta f \sin(\theta_o - \alpha)\right)^2$$

If $n\Delta f \sin(\theta_o - \alpha)$ is small compared to $f_o$, we may write

$$f \approx f_o + n\Delta f \cos(\theta_o - \alpha) \tag{9}$$

The largest $n\Delta f \sin(\theta_o - \alpha)$ may be is $(N-1)\Delta f \sin(\theta_o - \alpha)$. As shown in fig.4., this quantity is the component of the transform perpendicular to the radial direction. A small value compared to $f_o$ implies that the rotation angle change during the transform must be small. The rotation angle can be made small either by orienting the hybrid profile close to a down-range profile (make $\theta_o - \alpha$ small); or if this not possible, by keeping the actual length of the transform small (reduce $N\Delta f$). This approximation is desirable because f is a linear function of n, which allows one to interpret the hybrid profile as a tomographic projection.

With the approximation (9), equation (8) becomes

$$h(k) = DFT_N\left\{e^{j\frac{4\pi d}{c}f_o} \int_{x=-\infty}^{+\infty} \int_{y=-\infty}^{+\infty} g(x, y) e^{j\frac{4\pi}{c}\Delta f[d\cos(\theta_o - \alpha) - s]n} e^{-j\frac{4\pi}{c}f_o u} dxdy\right\} \tag{10}$$

To improve resolution, a window function is usually included in (10). Let $w(n)$ be the window function, and $W(\omega)$ be its discrete-time Fourier transform. ($W(\omega)$ is thus periodic with period $2\pi$.) Using the definition of the DFT, we write

17

$$h(k) = \sum_{n=0}^{N-1} \left\{ w(n)e^{-j\frac{2\pi}{N}nk} e^{j\frac{4\pi d}{c}f_o} \int_{y=-\infty}^{+\infty} \int_{x=-\infty}^{+\infty} g(x,y)e^{j\frac{4\pi}{c}\Delta f[d\cos(\theta_o - \alpha) - s]n} e^{-j\frac{4\pi}{c}f_o u} dxdy \right\}$$

$$= e^{j\frac{4\pi d}{c}f_o} \int_{y=-\infty}^{+\infty} \int_{x=-\infty}^{+\infty} g(x,y)e^{-j\frac{4\pi}{c}f_o u} \sum_{n=0}^{N-1} \left\{ w(n)e^{-j\frac{2\pi}{N}nk} e^{j\frac{4\pi}{c}\Delta f[d\cos(\theta_o - \alpha) - s]n} \right\} dxdy$$

$$= e^{j\frac{4\pi d}{c}f_o} \int_{y=-\infty}^{+\infty} \int_{x=-\infty}^{+\infty} g(x,y)e^{-j\frac{4\pi}{c}f_o u} W\left[ \frac{2\pi}{N}k + \frac{4\pi}{c}\Delta f(d\cos(\theta_o - \alpha) - s) \right] dxdy$$

Now let $\bar{W}(x) = W\left(\frac{4\pi\Delta f}{c}x\right)$. Note that $W$ is periodic with period $2\pi$, and W

bar is periodic with period $\frac{c}{2\Delta f}$. We have for $h(k)$

$$h(k) = e^{j\frac{4\pi d}{c}f_o} \int_{y=-\infty}^{+\infty} \int_{x=-\infty}^{+\infty} g(x,y)e^{-j\frac{4\pi}{c}f_o u} \bar{W}\left[ \frac{c}{2N\Delta f}k + d\cos(\theta_o - \alpha) - s \right] dxdy \qquad (11)$$

The double integral is in terms of the x-y coordinate system. Consider instead the rotated coordinate system (s,t) as given by

$$s = x \cos \alpha + y \sin \alpha$$
$$t = y \cos \alpha - x \sin \alpha$$

In the new system, u, the down-range location of a scatterer, will be given by

18

$$u(s, t) = s \cos(\alpha - \theta_o) + t \sin(\alpha - \theta_o) \; .$$

In the new system we have for h(k)

$$h(k) = e^{j\frac{4\pi d}{c}f_o} \int\limits_{s=-\infty}^{+\infty} \int\limits_{t=-\infty}^{+\infty} g(s, t) e^{-j\frac{4\pi}{c}f_o u} \bar{W}\left[\frac{c}{2N\Delta f}k + d\cos(\theta_o - \alpha) - s\right] dtds \tag{12}$$

The integration over t may be interpreted as a tomographic projection of a phase-shifted reflectivity density function. The tomographic projection, $p_\alpha(s)$, of g multiplied by the phase factor is given by the following integral:

$$p_\alpha(s) = \int\limits_{t=-\infty}^{+\infty} g(s, t) e^{-j\frac{4\pi f_o}{c}u(s, t)} dt \tag{13}$$

The integration occurs along lines parallel to the t axis, collapsing the phase-shifted g function onto the s axis. Note that the orientation of the s axis is identical to the orientation of the sequence of points in data space which are transformed to form the hybrid profile. Thus the orientation of the s axis is independent of the initial rotation angle, $\theta_o$. This is an advantageous property of the algorithm, in that the projection angle can be controlled arbitrarily by selecting different transform orientations in data space, without utilizing different initial rotation angles. It is this property which allows one to achieve great angular diversity in the projection angle while remaining at the same initial rotation angle, thereby utilizing a small rotation angle interval.

There is a simple physical interpretation of the exponential phase factor in (13). The phase shift on each part of g is proportional to u(s,t). The

19

geometric meaning of u, as shown in fig.1, is down-range position as measured from the origin. This phase shift is a manifestation of the time delay existing between scatterers separated in down range.

With this projection interpretation, h(k) becomes

$$h(k) = e^{j\frac{4\pi d}{c}f_o} \int\limits_{s=-\infty}^{+\infty} p_\alpha(s)\, \bar{W}\left[\frac{c}{2N\Delta f}k + d\cos(\theta_o - \alpha) - s\right] ds$$

The integration on s is a convolution between $p_\alpha(s)$ and W bar($d\cos(\theta_o-\alpha)+s$):

$$h(k) = e^{j\frac{4\pi d}{c}f_o}\left[p_\alpha(s) * \bar{W}(s + d\cos(\theta_o - \alpha))\right]\Bigg|_{\tau = \frac{c}{2N\Delta f}k} \tag{14}$$

The bracketed quantity is a function of delay ($\tau$) between the projection and the weighting function. The relation between the delay and k (the independent variable of the hybrid profile) is given above. Equation (14) shows that the hybrid projection $p_\alpha(s)$ is convolved with the transform of the DFT window, causing a reduction in resolution. Moreover, the window is delayed by $-d\cos(\theta_o-\alpha)$, causing ambiguity in the origin of the hybrid profile, by virtue of the fact that d is unknown. Although the loss of resolution can be ameliorated by an increase in the transform size, the origin ambiguity can cause problems, and is discussed in Chapter II.

To summarize, a hybrid profile is formed by transforming I-Q measurements along a line segment within the data space. The orientation of the segment determines the projection angle, which determines the direction of hybrid range. The hybrid profile is interpreted as a projection of a phase-shifted g(x,y) onto an axis with the same orientation as the transform in data space.

By considering (14), we see that transforming a segment in data space

20

effectively performs the following six operations:

1) The reflectivity density function, g(x,y), is phase shifted in proportion to down range.

2) The phase-shifted density function is tomographically projected at an angle $\alpha$ to form the one-dimensional projection $p_\alpha(s)$.

3) The above projection is convolved by the transform of the window weighting function, $W(\omega)$.

4) The convolved projection is shifted by $-d\cos(\theta_o-\alpha)$ mod $c/2\Delta f$.

5) The convolved, shifted projection is phase shifted by $e^{j\frac{4\pi f_o}{c}d}$.

6) The above projection is sampled every $c/2N\Delta f$ length units.

The phase shift is in proportion to the down-range position, and the tomographic projection is perpendicular to the direction of the data space transform. The hybrid profile is therefore quite similar to the tomographic projection of (1). The two significant differences are 1) g has been phase shifted before being projected (versus being projected only) and 2) the entire profile is shifted by $-d\cos(\theta_o-\alpha)$ mod $c/2\Delta f$. The first difference gives rise to speckle, and the second gives rise to the zero reference problem. These two phenomena must be corrected before convolution-backprojection can be used.

## Speckle Reduction

In high resolution radar imaging, a resolution cell may contain more than one scatterer. Although the scatterers are in the same resolution cell, they may have different down range positions, causing each scatterer in the cell to

have a different phase. However, the return provided by the radar is coherent sum of the scatterers' complex amplitudes, giving rise to constructive and destructive interference, known as <u>speckle</u>.

In our situation, each resolution cell is actually a strip. A given hybrid profile bin (resolution cell) may contain more than one scatterer, and we are therefore faced with the speckle problem for each strip-shaped hybrid profile bin.

Mathematically, speckle occurs because the formation of the hybrid profile involves a projection of a phase shifted g(s,t):

$$p_\alpha(s) = \int_{t=-\infty}^{+\infty} g(s,t) e^{-j\frac{4\pi f_o}{c} u(s,t)} \, ds$$

The phase factor involves u, which is down-range position, as shown in fig.2. Because the reflectivity density function is phase shifted in proportion to down range, scatterers within a hybrid profile bin give rise to speckle.

The classical approach to speckle reduction [6] can be used for hybrid profile speckle reduction as well. The classical method is to re-resolve the region of the target corresponding to the speckle-ridden resolution cell. This entails computing $p_\alpha(s)$ using several different initial frequencies $f_o$, and noncoherently averaging the resulting $p_\alpha(s)$ profiles. In our situation, L hybrid profiles are made using the same values of $\theta_o, \alpha, \Delta f, N$, etc., but different $f_o$; typical values of L are 5-15.

The next step involves the noncoherent averaging of the resulting L profiles. Fig.5 shows a typical set of L hybrid profiles which are averaged to reduce speckle within a single projection. The averaging is expressed mathematically as
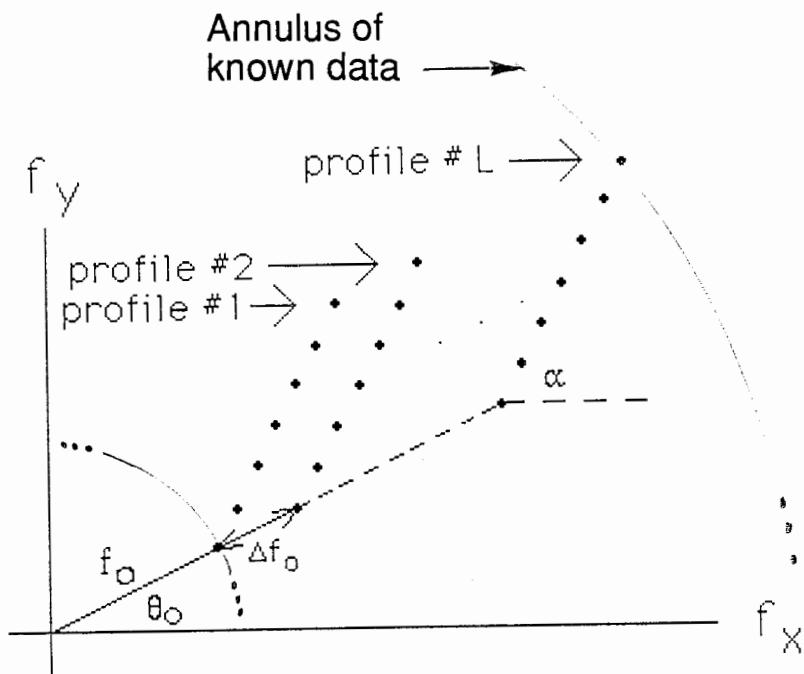
22

Figure 5. A set of hybrid profiles which are averaged to reduce speckle.

$$p_\alpha(k) = \frac{1}{L} \sum_{q=1}^{L} \left\| h_q(k) \right\|^2$$

$$= \frac{1}{L} \sum_{q=1}^{L} \left\| DFT_N \left\{ H(q\Delta f_o \cos \theta_o + f_{xo} + \Delta f_x \cdot n, \ q\Delta f_o \sin \theta_o + f_{yo} + \Delta f_y \cdot n) \right\} \right\|^2 \tag{15}$$

It can be shown that if a single resolution cell with scatterers $A_1, \ldots, A_k$ is resolved at frequencies $f_1, \ldots, f_L$ giving complex amplitudes $R_1, \ldots, R_L$, then

$$\lim_{L \to \infty} \frac{1}{L} \sum_{q=1}^{L} \left\| R_q \right\|^2 \propto \sum_{q=1}^{k} A_q^2$$

That is, averaging the squared magnitude of the returns gives the sum of the squared amplitudes of the scatterers in that cell [6,p1124-1209},[8]. Likewise, averaging the squared amplitude of the L hybrid profiles made at different values of $f_o$ produces a real function which is proportional to the tomographic projection of $g^2(x,y)$. To summarize the process, a segment in data space is windowed and transformed, then shifted so that the origin and center of rotation coincide. This is repeated L times at different values of $f_o$, and the resulting hybrid profiles are averaged noncoherently. This averaging is needed to eliminate the speckle present in each of the hybrid profile bins.

In addition to desensitization to the phase shift phenomenon, the noncoherent averaging is desired for a second reason. When collecting stepped frequency measurements of an actual target, the target cooperatively traverses a circular path. In doing so, it generates the desired yaw rotation. However,

as the craft traverses the circle, it will also undergo significant roll and pitch motion due to sea state or buffeting winds, in the case of a ship or aircraft respectively. Because of these effects, the rotation axis is different for each projection. (Note that with conventional ISAR over a $1$-$2^\circ$ rotation angle change, this problem is absent because the actual motion is well approximated by rotation about a single axis.) To desensitize to this variation in rotation axis, the final projection used in the convolution-backprojection algorithm is chosen to be the average of the squared magnitudes of the profiles. Thus, there are two motives in selecting noncoherent processing: desensitization to the phase shift phenomenon, and desensitization to variations in the rotation axis.

## The Zero Reference Problem

After forming the hybrid projections of the target's reflectivity density function, convolution-backprojection is applied to the projections to form an estimate of the reflectivity density function. However, the convolution-backprojection algorithm requires that the origin of each projection correspond to the same point on the target. With the processing used to form the hybrid profiles, this requirement is not met. The additional processing needed to insure that this requirement is met is described below.

Equation (14) gives a convolution between $p_\alpha(s)$, the projection of g, and the window's transform delayed by $-d\cos(\theta_0-\alpha)$. Since the window's transform is periodic, $p_\alpha(t)$ will actually be shifted by $-d\cos(\theta_0-\alpha)$ mod $c/2\Delta f$. Before the shift, $p_\alpha(\text{zero})$ corresponded to the center of rotation. What is needed is a way to shift $p_\alpha(s)$ back by $d\cos(\theta_0-\alpha)$ mod $c/2\Delta f$. Achieving this shift is complicated by the fact that d, the radar-target separation, is unknown. Instead of computing $-d\cos(\theta_0-\alpha)$ and modding by $c/2\Delta f$, the approach used here estimates $-d\cos(\theta_0-\alpha)$ mod $c/2\Delta f$ directly. This estimate begins with the formation of a plot of down-range profiles vs. rotation angle for the annular
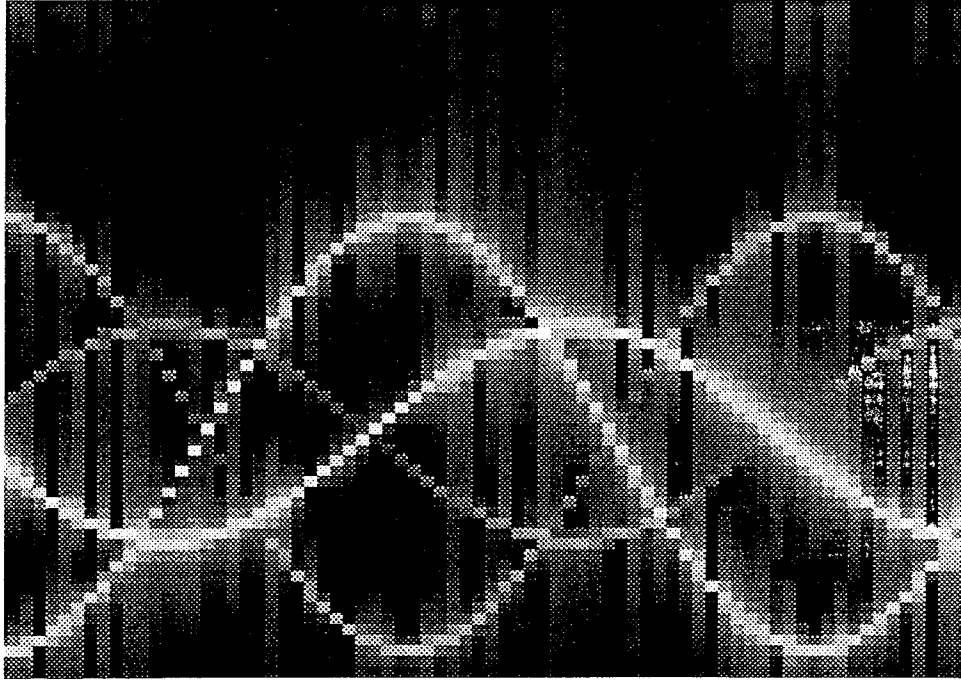
25

Figure 6. A typical plot of down-range profiles versus angle, showing the oscillation of four scatterers around the center of rotation.

region mentioned earlier. Such a plot shows the sinusoidal variation in down range position of each scatterer with rotation angle, as shown in fig.6. All the sinusoids have the same mean, which is the center of rotation. The estimate of $-d\cos(\theta_o-\alpha) \mod c/2\Delta f$ is the distance between the sinusoidal mean and the zero bin. Lastly, each profile is shifted back by this amount, so that the zero bin corresponds to the center of rotation.

The origin point on the target is chosen to be the center of rotation, because it is an easy point to locate on the target. However, when dealing with a live target, other points may be easier to use as a reference. For example, some techniques used for motion compensation of ISAR reflectivity data are designed to reference profiles to a strong scatterer on the target [1,9,10].


Tomographic Reconstruction

At this point, the formation of center-of-rotation aligned hybrid projections has been described. Typically 100-200 hybrid projections are formed using a wide range of $\alpha$ and $\theta_o$. Next, g', the estimate of $g^2$, is formed by applying convolution-backprojection to these projections.

Convolution-backprojection can be described as a two step process. First, each projection is discrete-time filtered with a high frequency enhancement filter (convolution step):

$$p'_{\alpha i}(k) = p_{\alpha i}(k) * f(k)$$

With

$$f(k) = \begin{cases} \frac{1}{4} \; ; \; k = 0 \\ 0 \; ; \; k \text{ even and } \neq 0 \\ -\frac{1}{(k\pi)^2} \; ; \; k \text{ odd} \end{cases}$$

The function $p_{\alpha i}$ is the speckle-reduced projection given in (15), made at projection angle $\alpha_i$. The function p' is the filtered projection, and f is the impulse response of the filter [7]. In the second step, the reconstructed image (g') is formed by summing the filtered projections as follows (backprojection step):

$$g'(x, y) = \sum_{i=1}^{M} p'_{\alpha i} (x \cos \alpha_i + y \sin \alpha_i) \qquad (16)$$

Interpolation is needed in (16), because $x\cos\alpha_i + y\sin\alpha_i$ may not correspond to an available value of $p_{\alpha i}(k)$.

The geometric interpretation of (16) is to consider each filtered projection convolved across the image plane at an angle of $\alpha-90°$. A single projection contributes equally to g' on a locus of points (x,y) which lie along a line perpendicular to the direction of transform in data space. For example, consider a down-range projection ($\alpha=90°$): each bin of the projection will contribute equally to a line (or strip) of constant down-range, and varying cross-range.

The convolution-backprojection method is further described in [7].

## Summary of Imaging Algorithm

The imaging algorithm is composed of six basic steps:

1) Collect I-Q reflectivity data in an annular region of $\theta$-f space for the target in question, as described in Chapter I.

2) Select and produce a pattern of hybrid projections using significant diversity in the projection angle. This selection consists of determining values of $L, f_o, \Delta f, N, \Delta f_o$ (which are common to all the projections), and $\alpha$, $\theta_o$ (which are specific to each projection). Various strategies of selecting these parameters are discussed under Experimental Results, Chapter III. The formation of projections using these parameters consists of five steps:

A) Using the values of $\alpha, \theta_o, f_o, \Delta f, \Delta f_o$, and N, obtain H(n) from the values of $H(f_x, f_y)$ from the annulus as follows:

$$H(n) = H\left[(f_o + q\Delta f_o)\cos \theta_{o_i} + n\Delta f \cos \alpha_i, (f_o + q\Delta f_o)\sin \theta_{o_i} + n\Delta f \sin \alpha_i\right]$$

The index q denotes the $q^{th}$ profile which will be incoherently averaged, to form the $i^{th}$ speckle-reduced hybrid projection which is used in the convolution backprojection step.

B) Window the sequence H(n) by forming the product:

$$w(n) \cdot H(n)$$

where w(n) is the length N window function. Then transform with an FFT:

$$FFT[w(n) \cdot H(n)]$$

C) Repeat 2A,2B L times for q=1,...,L. Then form the average

$$p_{\alpha i}(k) = \frac{1}{L} \sum_{q=1}^{L} \left\| FFT[w(n) \cdot H(n)] \right\|^2 \qquad 0 \le k \le N-1$$

D) Shift $p_{\alpha i}(k)$ so that the origin is coincident with the center of rotation, as described in Chapter II.

E) Repeat steps 2A-2D until all projections have been formed. We now have the projections:

$$p_{\alpha i}(k) \; ; \; i = 1,...,M$$

3) Apply convolution-backprojection to the projections to form the image.

A) Convolve each projection with the sequence:

$$f(k) = \begin{cases} \frac{1}{4} \; ; \; k = 0 \\ 0 \; ; \; k \text{ even and} \ne 0 \\ -\frac{1}{(k\pi)^2} \; ; \; k \text{ odd} \end{cases}$$

B) Reconstruct g' using

$$g'(x, y) = \sum_{i=1}^{M} p_i(x \cos \alpha_i + y \sin \alpha_i)$$

Interpolation is needed when $x\cos\alpha_i + y\sin\alpha_i$ is noninteger.

Resolution Limits of the Algorithm

A useful way of gauging the performance of a radar imaging algorithm is through its point spread function. The point spread function is defined as the image produced by the algorithm when the target is a single ideal point scatterer located at the origin. If g' is the estimate of $g^2(x,y)$ produced by the algorithm, then the algorithm may be described by a mapping from g to g':

$$g'(x, y) = A\{g(x, y)\}$$

The point spread function, r(x,y), is the image produced when $g(x,y) = \delta(x,y)$:

$$r(x, y) = A\{\delta(x, y)\}$$

The broadness and sidelobes of r(x,y) is a measure of how much distortion the algorithm produces when imaging a single point scatterer. The point spread function should ideally be a delta function, and the "closeness" of the point spread function to a delta function is a gauge of the algorithm's performance.

Using $g(x,y) = \delta(x,y)$ in (14), we have for h(k):

$$h(k) = e^{j\frac{4\pi d}{c}f_o} \cdot W\left(\frac{c}{2N\Delta f}k + d\cos(\theta_o - \alpha)\right)$$

Next, we form hybrid profiles using different values of $f_o$, then average them noncoherently to produce the samples of a projection of $g^2$. This is

31

expressed as:

$$p_\alpha(k) = \frac{1}{L} \sum_{q=1}^{L} \left\| h_q(k) \right\|^2$$

$$= \frac{1}{L} \sum_{q=1}^{L} \left\| e^{j\frac{4\pi d}{c}f_q} \cdot W\left(\frac{c}{2N\Delta f}k + d\cos(\theta_o - \alpha)\right) \right\|^2$$

$$= \frac{1}{L} \sum_{q=1}^{L} \left\| W\left(\frac{c}{2N\Delta f}k + d\cos(\theta_o - \alpha)\right) \right\|^2$$

$$= W^2\left(\frac{c}{2N\Delta f}k + d\cos(\theta_o - \alpha)\right)$$

Next, the projection $p_\alpha(k)$ is aligned to the origin. The origin-aligned projection is given by

$$W^2\left(\frac{c}{2N\Delta f}k\right)$$

Next, the projection is filtered with the high-frequency enhancement filter, so that the filtered projection is given by

$$p'_\alpha(k) = W^2\left(\frac{c}{2N\Delta f}k\right) * f(k)$$

From the above expression, p′ is $\alpha$-independent. This is not surprising, because g is rotationally symmetric. Using (16), we have for r(x,y):

$$r(x, y) = \sum_i p' \left[ x \cos(\alpha_i) + y \sin(\alpha_i) \right] \qquad (17)$$

It is known that the wider the spacing between the $\alpha_i$ values, the more distorted the point spread function [7]. Let us assume the best possible case, where an infinitude of projections are spaced infinitesimally closely over $180^\circ$. Assuming p' is perfectly interpolated, the sum of (17) becomes an integral:

$$r(x, y) = \int_0^\pi p' \left[ x \cos \alpha - y \sin \alpha \right] d\alpha$$

Let us write r in polar coordinates

$$r(R, \phi) = \int_0^\pi p' \left[ R \cos \phi \cos \alpha + R \sin \phi \sin \alpha \right] d\alpha$$

$$= \int_0^\pi p' \left[ R \cos(\alpha - \phi) \right] d\alpha$$

With

$$x = R \cos \phi$$
$$y = R \sin \phi$$

The function r is circularly symmetric. Thus $r(R,0) = r(R,\phi)$, and

33

$$r(R, \phi) = r(R) = \int_0^\pi p' [R \cos \alpha] d\alpha$$

With

$$p'(s) = \text{interpolated} \left[ W^2 \left( \frac{c}{2N\Delta f} k \right) * f(k) \right]$$

This integral is typically intractable, and numerical methods must be used to calculate r(R).

   The window weighting function used in this paper to form hybrid profiles is the Kaiser-Bessel window. Fig.7 shows a plot of r(R) for the Kaiser-Bessel window ($\beta=2$). The point spread function plot has a narrow main lobe and sidelobes which  indicate that this algorithm is theoretically capable of producing accurate estimates of the target's RCS distribution.
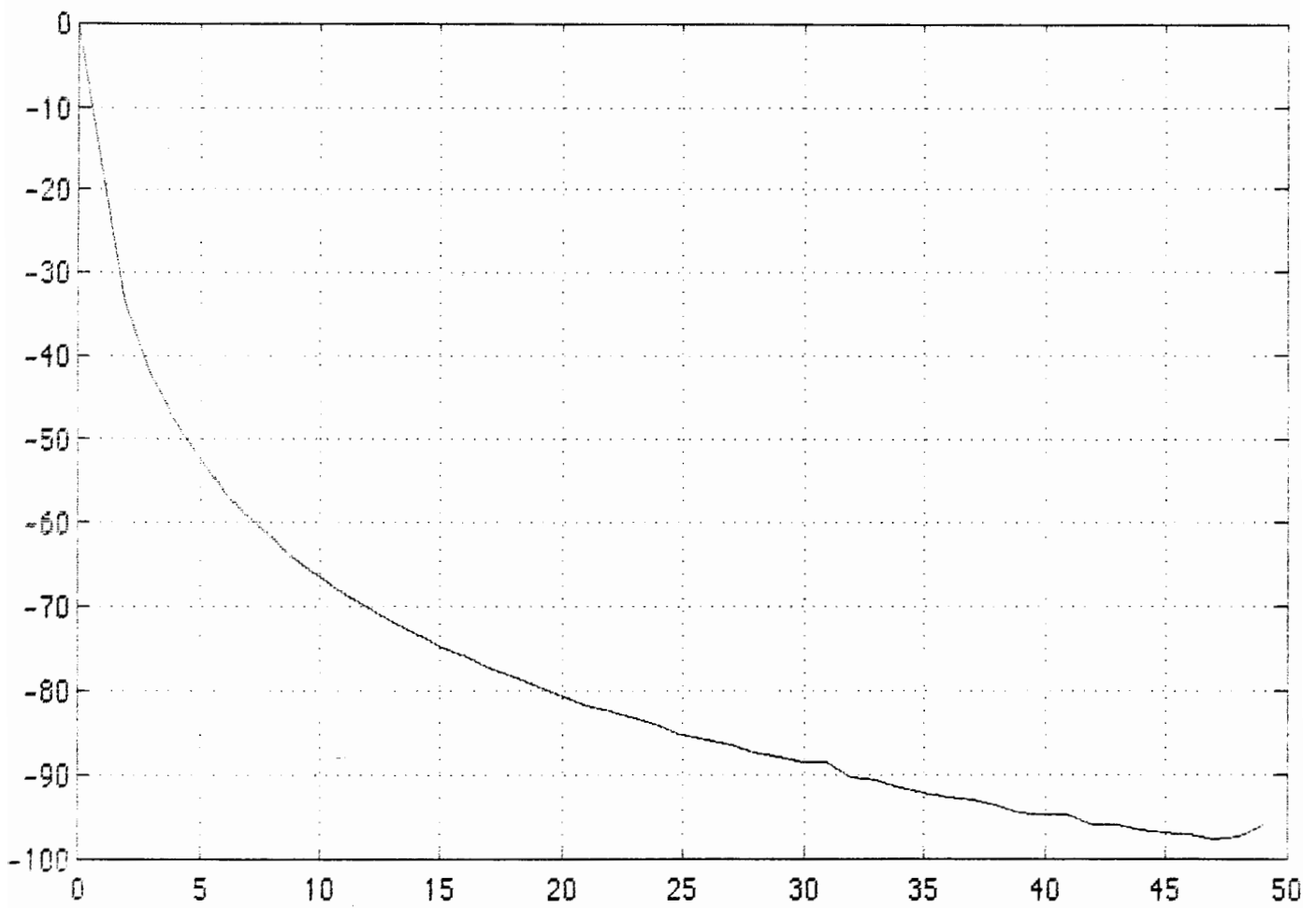
Figure 7. The point spread function in decibels versus normalized length.

# CHAPTER III

## EXPERIMENTAL RESULTS

In this section, images of a simulated target and of a turntable model are presented.

### Simulated Target

The purpose of this simulated target example is to verify the proper functioning of the algorithm implementation; therefore, a simple configuration of projections is used. Fig.8 shows the positions of the scatterers making up the simulated target. This configuration consisted of eighty projections with $\theta_o=0^o,\ldots,177.75^o$ in increments of $2.25^o$, with corresponding $\alpha=0+90^o,\ldots,177.75^o+90^o$. Since $\alpha=\theta_o+90^o$, the projections are cross-range projections. For each projection, L=20 profiles were averaged using different initial radial frequencies corresponding to $f_o, f_o+\Delta f_o,\ldots,f_o+19\Delta f_o$. These profiles were then averaged to produce the hybrid projection. This method of imaging scatterers with cross-range profiles is the method used in [5]. The result is shown in Fig.9. The scatterers are well-resolved and correspond to their actual locations and amplitudes, indicating that the algorithm is functional and can form useful images of simulated data using a wide rotation angle.

Fig.10 is an image of the same three scatterers made using a configuration of 80 projections. The values of $\theta_o$ used were
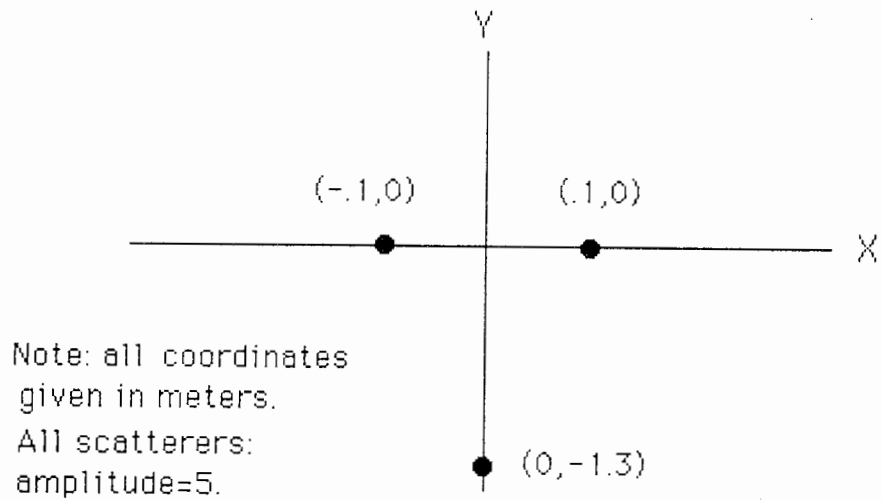
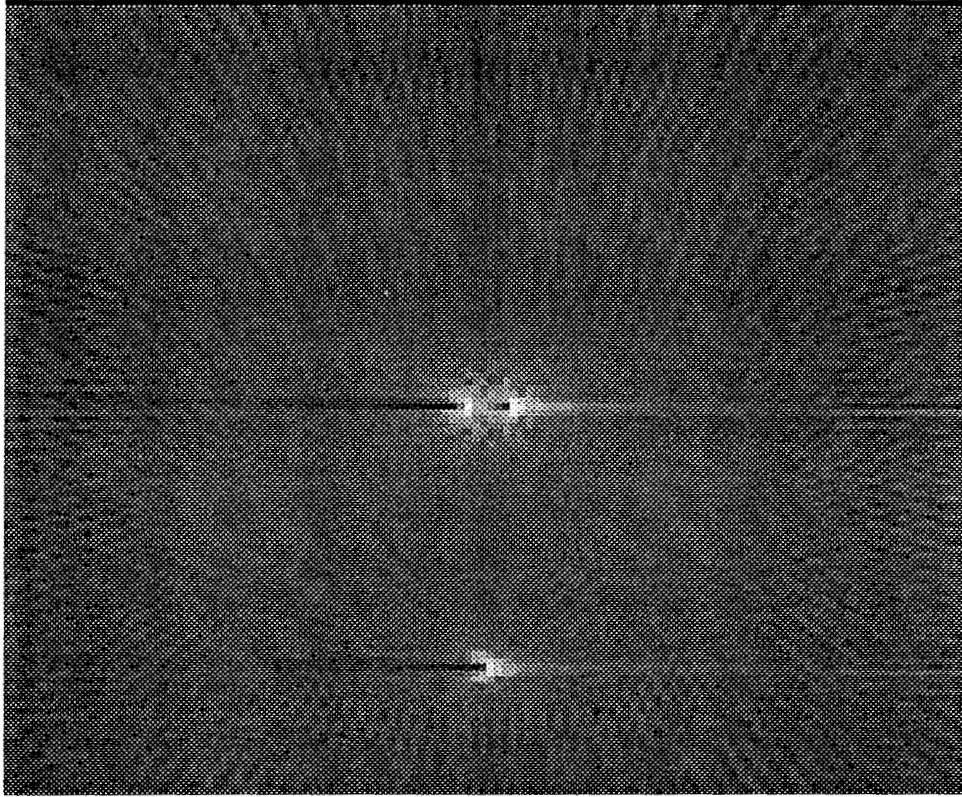Figure 8. The actual locations and strengths of the scatterers of the simulated target.

Figure 9. Image of the simulated target shown in fig.8, using method in [5]. In this case, M=80, N=128, L=20, $\Delta f$=38 MHz, $\Delta f_O$=38 MHz, $f_O$=24 GHz.

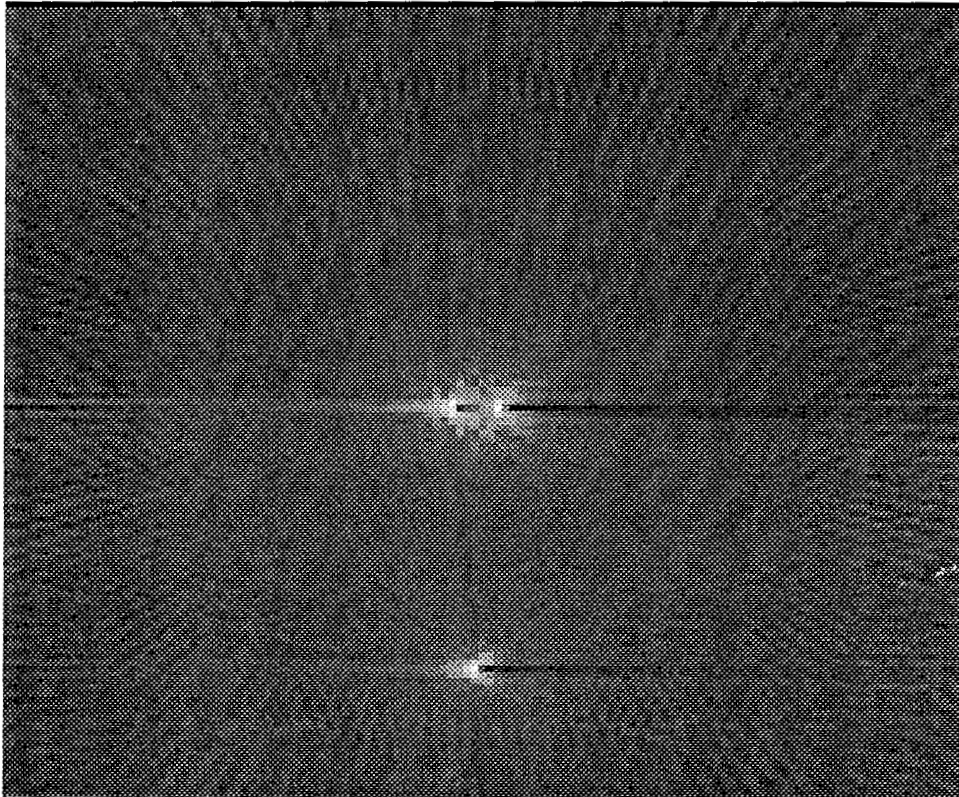Figure 10. Image of simulated target shown in figure 8. Values of M,N,L,$\Delta f$,$\Delta f_O$, and $f_O$ are the same as in figure 9. Values of $\alpha$ are the same as in fig.9, but values of $\theta_O$ are different.
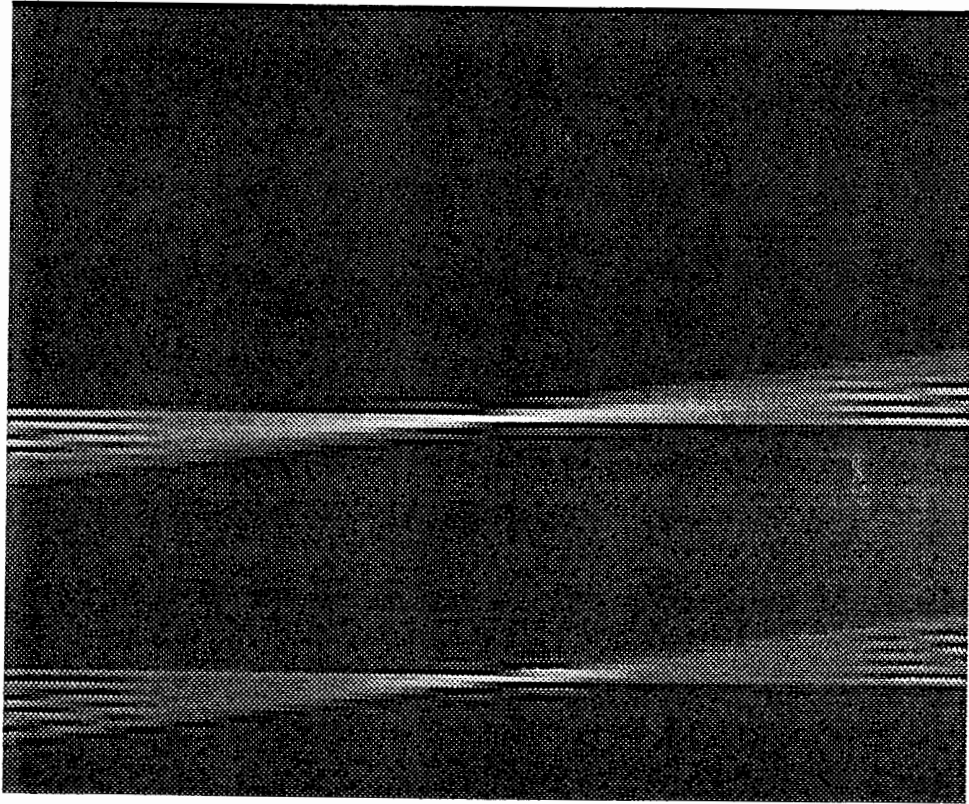
Figure 11. Image of simulated target shown in fig.8 using method in [5]. Values of $M,N,L,\Delta f,\Delta f_o$, and $f_o$ are the same as in fig.9. Only $10^o$ of rotation angle is used in this case.

$$\theta_o=0^o,2.25^o,4.5^o,6.75^o,9.0^o.$$

At each value of $\theta_o$, 16 projections were made with

$$\alpha=\theta_o-90^o+i(11.25^o) \; ; \; i=0,\ldots,15$$

were made. The values of M,N,L,$\Delta f$,$\Delta f_o$,and $f_o$ are the same as the previous image in fig.9. As before, 20 hybrid profiles made at different radial frequencies were averaged to form each projection.

The values of $\alpha$ used in fig.9 and 10 are identical, but the corresponding values of $\theta_o$ are different. Because the values of $\alpha$ are the same, the images are very similar. This image demonstrates that with a suitable configuration of hybrid profiles, this algorithm can be used to successfully image simulated targets.

Fig.11 is an image of the simulated target made with

$$\theta_o=0^o,2.25^o,4.5^o,6.75^o,9.0^o.$$

At each value of $\theta_o$, one projection was made with $\alpha=\theta_o+90^o$.This configuration is the same as that used in fig.9, but the rotation angle is only $10^o$. There is a very small diversity in $\alpha$, the projection angle. As expected, the three scatterers are very poorly resolved and the image quality is very poor. By comparing fig.10 and fig.11, which both use the same rotation angle swath, we see a vast improvement in the hybrid profile method (fig.10) as compared to the method of [5] (fig.11).

Turntable Model Experiment

Next we present the results of the algorithm applied to compact range measurements of a scale model aircraft. The turntable model is a one-seventh scale model of an A4 tactical aircraft. The target was rotated on a turntable, and the annulus of data was collected as described in Chapter I. The inner radius of the annulus is 24 GHz, and its frequency bandwidth is 2.37 GHz. The polarization used is HH.

There is one important difference between model targets and simulated targets. On model targets, scattering centers exist over small angular intervals ($5-30^{\circ}$). As the rotation angle is changed, a given scatterer may become reflective for a $5-30^{\circ}$ interval, then disappear. The reason for this is due to the geometry of the target: often a strong reflection can only result from a radar signal incident from a particular angle. Because an actual target's scattering centers exist for a limited rotation angle, a wide diversity of projection angles must be obtained over that interval to properly image the scatterers present in the interval. By contrast, the scatterers of simulated targets stay constant through the full $360^{\circ}$ circle.
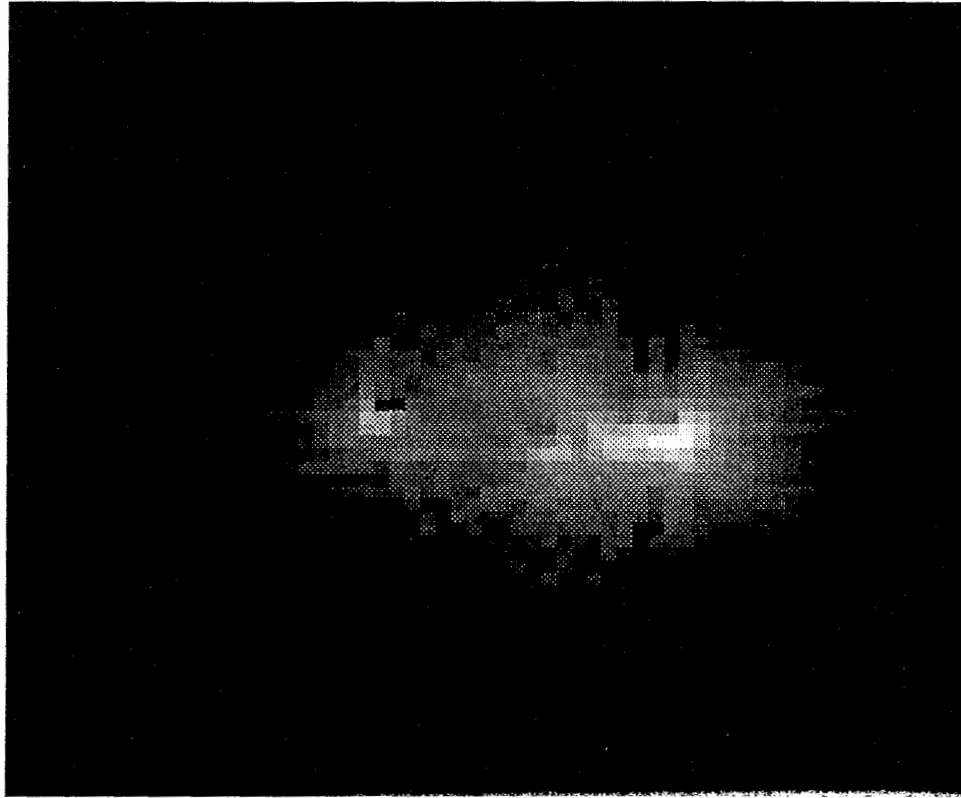
Fig.12a is an image of the A4 aircraft made using M=3600 projections. Sixty different initial rotation angles were used
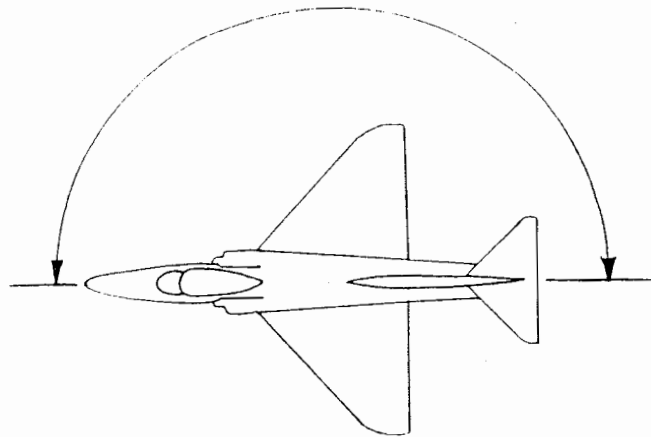
$$\theta_o = 10 + i(3^{\circ}) \; ; \; i = 0, \ldots, 59$$

For each value of $\theta_o$, sixty values of $\alpha$ were used:

$$\alpha = \theta_o - 90^{\circ} + i(3^{\circ}) \; ; \; i = 0, \ldots, 59$$

This hybrid profile configuration uses wide rotation angle ($\theta_o = 10^{\circ}$ to $190^{\circ}$),
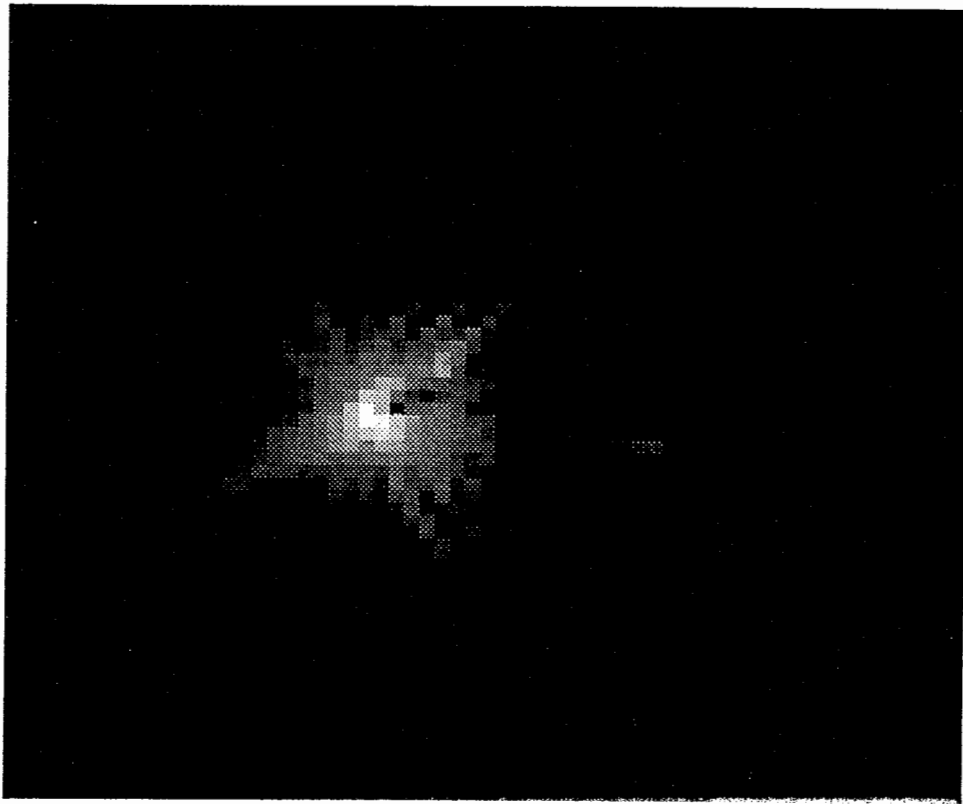
42

Figure 12a. Image of the A4 model. Values of $N, L, \Delta f, f_O, \Delta f_O$ are the same as in fig.9. A large ($180^O$) rotation angle was used. Figure 12b shows orientation and scale of fig.12a.

and a wide projection angle ($180^{\circ}$) for every $3^{\circ}$ of rotation angle. Therefore, this image should locate the scatterers on the target regardless of the angular interval over which the scatterer may occur.

Fig.12b shows the orientation of the A4 craft in fig.12a, as well as the interval over which the image was made. This image shows two main scattering centers. The scatterer near the nose corresponds to the engine inlet. The scatterer near the tail is due to the exhaust orifice at the tail. Although the A4 has other scatterers, they are not apparent in fig.12a. The reason is that the convolution-backprojection algorithm causes a scatterer's strength in the image to be proportional to both its amplitude and the duration of the angular interval over which it exists. Both the air inlet and exhaust orifice give rise to scatterers which appear for very long angular intervals. These two scatterers tend to drown out the other scatterers by comparison. This weighting of the scatterers in proportion to their duration of existence is useful when attempting to identify strong scatterers over a large interval. However, centers existing over smaller intervals are not visible.

In fig.12a, only one hybrid profile was "averaged" noncoherently ($L=1$) to form a given projection. While holding all other parameters fixed, $L$ was varied to 5,10, and 15. The image produced for these different values of $L$ showed insignificant differences, indicating that for this target, the number of hybrid profiles averaged to form the projection has little influence on the image. The reason for this is the A4 model has one or at most two scatterers present at a given angular interval. Because the scatterers are so sparse, there is little opportunity for destructive and constructive interference. In other words, there is little speckle, so there is little need to average. In light of this, the simulated data which also has very sparse scatterers, would also produce the same image quality, regardless of the value of $L$. However, when imaging a full scale live target, which have many scatterers (20+), a large value of $L$ should be used.

a
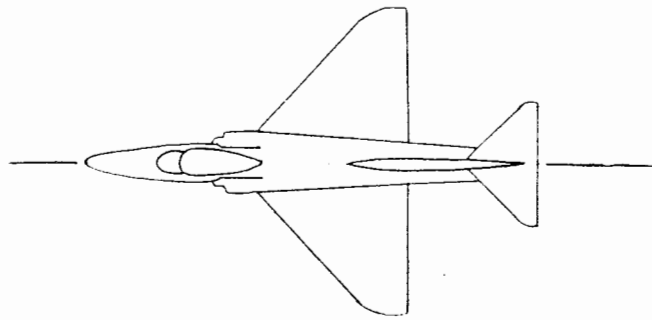


b

Figure 13a. Image of the A4 model. Values of $N, L, \Delta f, f_o, \Delta f_o$ are the same as in fig.9. Only $10^o$ of rotation angle was used. Figure 13b shows orientation and scale of fig.13a.

Fig.13a shows an image of the A4 aircraft made using M=300 projections. Five initial rotation angles were used

$$\theta_o=20^o,22^o,24^o,26^o,28^o.$$

For each value of $\theta_o$, 60 values of $\alpha$ were used:

$$\alpha=\theta_o-90^o+i(3^o) \quad ; \quad i=0,\ldots,59$$

The number of projections is the product of the number of rotation angles with the number of projections at each rotation angle. (M=5x60=300). This image uses a small rotation angle change ($\sim10^o$, neglecting the additional rotation angle due to the projections at $\theta_o=20,28^o$ near the edges), but a very wide projection angle interval ($180^o$). Therefore, this algorithm is designed to locate the scatterers existing in the angular interval from $20^o$ to $30^o$.

From fig.13a, we see that there is only one scatterer on the target in the $20-30^o$ rotation angle interval. This scatterer corresponds to the engine inlet, and is the same scatterer as the left-hand scatterer in fig.12a. This image demonstrates the ability of the algorithm to locate scatterers on the plane, and ascribe an interval over which the scatterer exists.

If it is desired to identify the scatterers' locations regardless of the length of their intervals, it is best to make several images similar to fig.13a, using different angular intervals. Each image would cover only $10^o$ or so, but it would indicate the strong scatterers on the target, regardless of how long a given scatterer was active. Using many such images over different angular intervals would allow all the scatterers on the target to be identified. As an example of this approach, fig.14a shows another image of the

46
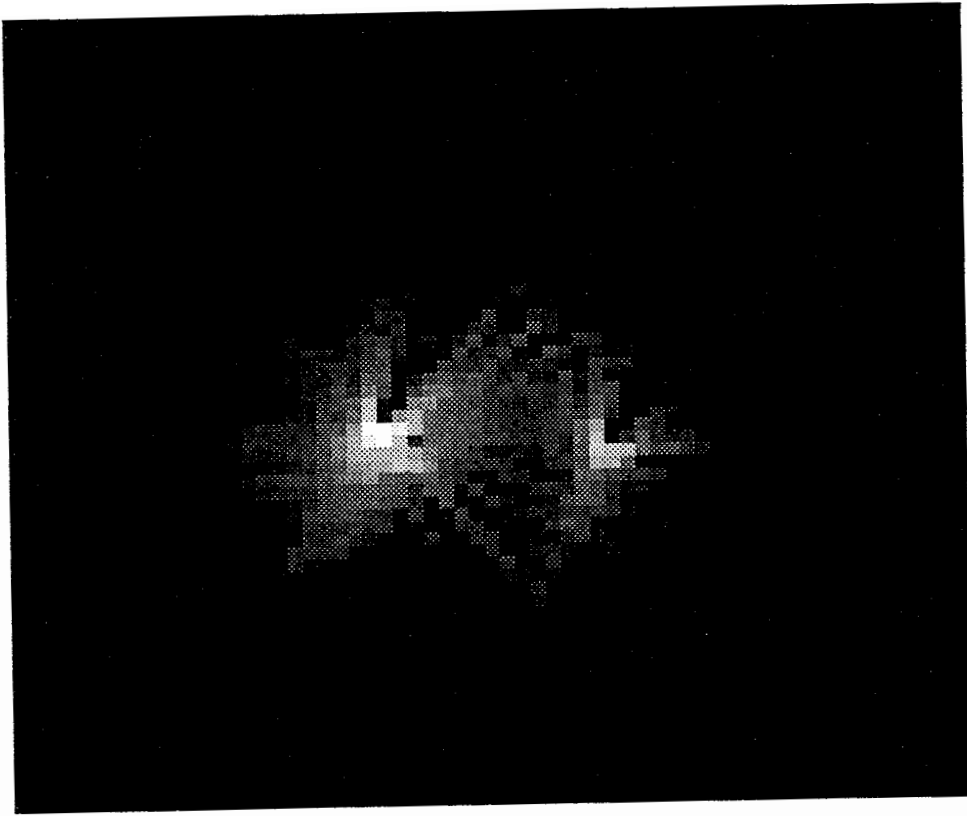
a
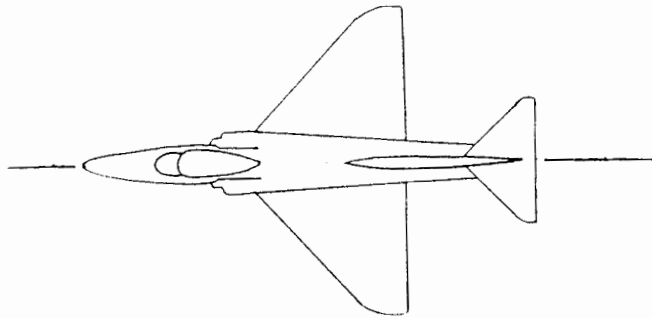


b

Figure 14a. Image of the A4 model. Values of N,L,$\Delta f$,$f_o$, $\Delta f_o$ are the same as in fig.9. Only $10^o$ of rotation angle was used. Figure 14b shows orientation and scale of fig.14a.

A4 model similar to fig.13a, covering a small angular interval. Values of $\theta_o$ are

$$\theta_o=60,62,64,66,68^o.$$

For each value of $\theta_o$, 60 projections were made using

$$\alpha=\theta_o-90^o+i(3^o) \quad ; \quad i=0,\ldots,59$$

These parameters are identical to fig.13a, except the interval $\theta_o$ from $60^o$ to $70^o$ was used instead of $20^o$ to $30^o$. This image shows two scatterers. The scatterer on the left towards the nose is the same scatterer shown in fig.13a, and is due to the engine inlet. The other scatterer in fig.14a, but not in fig.13a, is due to a glint from the models tail section. This image demonstrates the capability of the algorithm to identify a scatterer's location regardless of how long it is active.

CHAPTER IV

CONCLUSION


In this paper, we have demonstrated a method of forming radar images which locates and quantifies a target's scattering centers. This algorithm can process a wide-rotation-angle data swath, and is able to identify the scatterers, regardless of the angular interval over which the scatterers appear. Using the concept of a hybrid profile, this method forms tomographic projections of the target's reflectivity density function. The image is then formed by applying the convolution-backprojection reconstruction algorithm.

This method has been applied to both simulated targets and a scale turntable model. The images thus generated established the algorithm's capability to locate scattering centers over a wide rotation angle ($180^\circ$). In forming images of simulated targets, the algorithm's capability of imaging scatterers while using only a $15^\circ$ interval was also successfully demonstrated.

The A4 aircraft turntable model was imaged with this algorithm in two different ways. In the first method, the model was imaged using a wide of rotation angle ($180^\circ$), with a wide diversity in the projection angle. The strength of the scatterers on the resulting image was proportional to both the actual amplitude of the scatterers and the width of the angular interval over which the scatterers were active. The image generated with this method identified two scatterers which were present over $60^\circ+$ interval, but missed

the remaining scatterers which existed over smaller intervals. This method is most useful for locating and gauging the centers according to their amplitude and duration of existence in rotation angle.

In the second method, the model was imaged using a more narrow rotation angle ($\sim 10^{\circ}$) and a wide diversity in projection angle. The images generated with this method are useful for locating the scatterers on the target and estimating their amplitudes. Because only $10^{\circ}$ of rotation angle is used, the scatterers appearing in the image are known to lie within the $10^{\circ}$ interval. Therefore, this method can also identify a scatterer's location in rotation angle. This method is most useful for locating and quantifying the centers according to their amplitudes, and identifying the rotation angle interval over which the scatterers are most active. Moreover, this method can be extended by using several such images over separate rotation angles, so that all the scatterers may be identified, regardless of the angular interval over which the are present.

LIST OF REFERENCES

[1]   D. R. Wehner, *High Resolution Radar*. Norwood, MA: Artech House, 1987.

[2]   J. D. Kraus, *Electromagnetics*. McGraw-Hill, Inc., 1984.

[3]   F. J. Harris, "SAR and ISAR Signal Processing," Proc. SPIE, San Diego, CA, Sept. 1986.

[4]   F. J. Harris, "Overview of Radar Imaging (SAR and ISAR)," Proc. Radarcon 90, Adelaide, Australia, April 1990.

[5]   D. U. Gerlach, "Radar Cross Section (RCS) Measurements Using a Tomographic Inverse Synthetic Aperture Radar (ISAR) Algorithm," Proc. Radarcon 90, Adelaide, Australia, April 1990.

[6]   C. Elachi, et al. "Spaceborne Synthetic Techniques and Technology," Proc. IEEE, Vol. 20, No.10, Oct. 1982.

[7]   A. Kak, "Principles of computerized Tomography," Tech. Report, Purdue University, 1984.

[8]   D. M. McDonald, "Speckle Reduction in Synthetic Aperture Radar Images," DSTO/SRL Technical Memorandum SRL-0010-TM. DSTO, Salisbury, South Australia, 1988.

[9]   B. Haywood, and R. J. Evans,  "Motion Compensation for ISAR imaging," Proc.  Australian Symposium on Signal Processing and Applications. P.113-117, 1989.

[10]  S. E. Simmons, "Kalman Range Tracking for ISAR Motion Compensation," Proc. Radarcon 90, Adelaide, Australia, April 1990.